

See discussions, stats, and author profiles for this publication at: <https://www.researchgate.net/publication/26670228>

# Reaction Dynamics of O(D-1,P-3) + OCS Studied with Time-Resolved Fourier Transform Infrared Spectroscopy and Quantum Chemical Calculations

ARTICLE in THE JOURNAL OF PHYSICAL CHEMISTRY A · JULY 2009

Impact Factor: 2.69 · DOI: 10.1021/jp903976z · Source: PubMed

---

CITATIONS

5

---

READS

8

6 AUTHORS, INCLUDING:



Hsin-Tsung Chen

Chung Yuan Christian University

78 PUBLICATIONS 703 CITATIONS

SEE PROFILE

# Reaction Dynamics of $O(^1D, ^3P) + OCS$ Studied with Time-Resolved Fourier Transform Infrared Spectroscopy and Quantum Chemical Calculations<sup>†</sup>

Hung-Chu Chiang, Niann-Shiah Wang, and Soji Tsuchiya\*

Department of Applied Chemistry and Institute of Molecular Science, National Chiao Tung University, Hsinchu 30010, Taiwan

Hsin-Tsung Chen

National Center for High-Performance Computing, No. 28, Nan-Ke Third Road, Hsin-Shi, Tainan, 74147, Taiwan

Yuan-Pern Lee\*

Department of Applied Chemistry and Institute of Molecular Science, National Chiao Tung University, Hsinchu 30010, Taiwan, and Institute of Atomic and Molecular Sciences, Academia Sinica, Taipei 10617, Taiwan

M. C. Lin\*

Department of Applied Chemistry and Institute of Molecular Science, National Chiao Tung University, Hsinchu 30010, Taiwan, and Department of Chemistry, Emory University, Atlanta, Georgia 30322

Received: April 30, 2009; Revised Manuscript Received: June 4, 2009

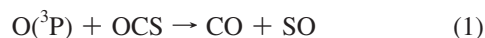
Time-resolved infrared emission of  $CO_2$  and  $OCS$  was observed in reactions  $O(^3P) + OCS$  and  $O(^1D) + OCS$  with a step-scan Fourier transform spectrometer. The  $CO_2$  emission involves  $\Delta v_3 = -1$  transitions from highly vibrationally excited states, whereas emission of  $OCS$  is mainly from the transition  $(0, 0^0, 1) \rightarrow (0, 0^0, 0)$ ; the latter derives its energy via near-resonant V–V energy transfer from highly excited  $CO_2$ . Rotationally resolved emission lines of  $CO$  ( $v \leq 4$  and  $J \leq 30$ ) were also observed in the reaction  $O(^1D) + OCS$ . For  $O(^3P) + OCS$ , weak emission of  $CO_2$  diminishes when Ar is added, indicating that  $O(^3P)$  is translationally hot to overcome the barrier for  $CO_2$  formation. The band contour of  $CO_2$  agrees with a band shape simulated on the basis of a Dunham expansion model of  $CO_2$ ; the average vibrational energy of  $CO_2$  in this channel is 49% of the available energy. This vibrational distribution fits with that estimated through a statistical partitioning of energy  $E^* \cong 18\,000 \pm 500\text{ cm}^{-1}$  into all vibrational modes of  $CO_2$ . For the reaction of  $O(^1D) + OCS$ , approximately 51% of the available energy is converted into vibrational energy of  $CO_2$ , and a statistical prediction using  $E^* \cong 30\,000 \pm 500\text{ cm}^{-1}$  best fits the data. The mechanisms of these reactions are also investigated with the CCSD(T)/6-311+G(3df)//B3LYP/6-311+G(3df) method. The results indicate that the triplet  $O(^3P) + OCS(X^1\Sigma^+)$  surface proceeds via direct abstraction and substitution channels with barriers of 27.6 and 36.4  $\text{kJ mol}^{-1}$ , respectively, to produce  $SO(X^3\Sigma^-) + CO(X^1\Sigma^+)$  and  $S(^3P) + CO_2(X^1A_1)$ , whereas two intermediates, OSCO and SC(O)O, are formed from the singlet  $O(^1D) + OCS(X^1\Sigma^+)$  surface without barrier, followed by decomposition to  $SO(a^1\Delta) + CO(X^1\Sigma^+)$  and  $S(^1D) + CO_2(X^1A_1)$ , respectively. For the ground-state reaction  $O(^3P) + OCS(X^1\Sigma^+)$ , the singlet–triplet curve crossings play important roles in the observed kinetics and chemiluminescence.

## Introduction

The reaction of oxygen atom with carbonyl sulfide ( $OCS$ ) is important in atmospheric chemistry, especially in the stratosphere in which ozone is a key constituent; the concentration of ozone is determined by a balance in a complicated photochemical reaction mechanism including reactions of  $O$  atoms in its electronically excited and ground states. Because  $OCS$  is relatively stable in the troposphere, it might enter the stratosphere to undergo photodissociation or reactions with other active species. Reactions of  $O$  atoms with  $OCS$  thus play a role

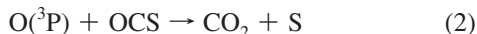
in balancing the  $O_3$  concentration and the radiation in the stratosphere.<sup>1</sup>

Several kinetic studies of the reaction  $O(^3P) + OCS$  have been reported; the rate coefficients are mostly in accord with recommendations by Atkinson et al.,  $k = 1.6 \times 10^{-11} \exp(-17.9\text{ kJ mol}^{-1}/RT)\text{ cm}^3\text{ molecule}^{-1}\text{ s}^{-1}$  for the temperature range 230–500 K,<sup>2</sup> and Singleton and Cvetanović,  $k = 7.80 \times 10^{-11} \exp(-21.8\text{ kJ mol}^{-1}/RT)\text{ cm}^3\text{ molecule}^{-1}\text{ s}^{-1}$  for the temperature range 230–1900 K.<sup>3</sup> From their discharge–flow experiments, Homann et al. proposed that of these two possible channels



<sup>†</sup> Part of the “Robert W. Field Festschrift”.

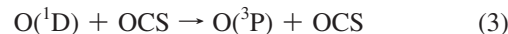
\* To whom correspondence should be addressed. E-mail: sojitsuchiya@mail.nctu.edu.tw (S.T.); yplee@mail.nctu.edu.tw (Y.-P.L.); chemmcl@emory.edu (M.C.L.).



the S-atom abstraction channel, reaction 1, dominates near room temperature.<sup>4</sup> Hsu et al. performed experiments with  $^{18}\text{O}(^3\text{P})$  at 298 K and found no product of  $\text{C}^{18}\text{O}$ , supporting the fact that the reaction proceeds via direct S-atom abstraction.<sup>5</sup> At temperatures above 1000 K, reaction 2 becomes important. Isshiki et al.<sup>6</sup> directly observed the time-dependent concentrations of both O and S atoms upon pulsed UV photolysis of mixtures of OCS and  $\text{SO}_2$  behind shock waves and determined rate coefficients of these two channels that yield a branching fraction of reaction 2 to be expressed as  $(0.40 \pm 0.10) - (202 \pm 137)/T$  in the temperature range of 1120–1540 K. They also performed quantum chemical calculations on this system with G2M(CC1) and CCSD-based G3 methods. The rate coefficients they derived by using transition-state theory (TST) with Wigner tunneling corrections are much smaller than experimental values; in contrast, the predicted branching ratios are similar to experimental values.

Rochford et al. performed crossed molecular beam experiments on  $\text{O}(^3\text{P}) + \text{OCS} \rightarrow \text{SO} + \text{CO}$  and found that the fraction of translational energy is  $\sim 30\%$  of the available energy.<sup>7</sup> They proposed that the cone-shaped scattering of SO arises from direct dissociation of an early transition state that is formed by a broadside approach of the O atom to the S atom of the OCS molecule; the reaction occurs over a triplet potential energy surface (PES) involving planar cis or trans bent intermediates; an extensive product rotational excitation is consequently expected. Shortridge and Lin employed resonance absorption with a CO laser to detect the vibrational population of CO product from mixtures of  $\text{NO}_2/\text{OCS}/\text{SF}_6$  upon UV ( $\lambda > 300$  nm) photolysis and reported CO ( $v \leq 4$ ) with a vibrational temperature of 9500 K, corresponding to 11% of the available energy.<sup>8</sup> In contrast, Nickolaissen et al. investigated the reaction  $\text{O}(^3\text{P}) + \text{OCS}$  with photolysis of mixtures of  $\text{NO}_2$  and OCS at 355 nm and detected CO product with a tunable IR laser. They observed CO in levels only  $v = 0$  and 1 with a ratio  $[\text{CO}(v = 1)]/[\text{CO}(v = 0)] \cong 0.05$ , whereas CO is rotationally excited with a temperature of 4400 K.<sup>9</sup> Their results indicate a mechanism of direct attack of  $\text{O}(^3\text{P})$  at the S atom of OCS, followed by rapid C–S bond scission that exerts a large torque on the CO fragment. Chen et al. employed laser-induced fluorescence to determine the internal state distribution of  $\text{SO}(X^3\Sigma^-)$  from the reaction  $\text{O}(^3\text{P}) + \text{OCS}$  and found that the SO product is highly vibrationally excited ( $v \leq 9$ ) with an inverted state distribution showing a maximum at  $v = 5$ .<sup>10</sup> The total internal energy amounts to about 50% of the available energy, with 26.0 and 8.1% converted to vibration and rotation of SO, and 0.6 and 15.7% to vibration and rotation of CO, respectively. This distribution was explained with a Franck–Condon model based on a mechanism of sudden separation of SO from the collision intermediate OSCO.<sup>11</sup>

The reaction of  $\text{O}(^1\text{D}) + \text{OCS}$  is little studied. Gauthier and Snelling reported the rate coefficient to be  $3.0 \times 10^{-10} \text{ cm}^3 \text{ molecule}^{-1} \text{ s}^{-1}$  at 300 K.<sup>12</sup> The electronically excited state  $\text{O}(^1\text{D}_2)$  is located  $15\,867.86 \text{ cm}^{-1}$  above the ground state  $\text{O}(^3\text{P}_2)$ .<sup>13</sup> Previously,<sup>14</sup> the authors reported that in the quenching reaction of  $\text{O}(^1\text{D})$  by  $\text{CO}_2$ , which proceeds through a collision complex  $\text{CO}_3$ , the product  $\text{CO}_2$  is highly vibrationally excited, with 44 and 5% of the available energy converted to vibrational and rotational degrees of freedom of product  $\text{CO}_2$ , respectively. OCS is isoelectronic with  $\text{CO}_2$ , but the bond energy of  $\text{C}=\text{S}$  is much smaller than that of  $\text{C}=\text{O}$ ; consequently, in addition to the quenching reaction



two reaction channels might occur



Jones and Taube irradiated an  $\text{O}_3/\text{OCS}/\text{Ar}$  matrix with UV light and observed CO,  $\text{CO}_2$ ,  $\text{SO}_2$ , and  $\text{SO}_3$  as products, indicating the existence of both reactions 4 and 5.<sup>15</sup> They also performed experiments with  $^{18}\text{O}_3/^{16}\text{OCS}/\text{Ar}$  and  $^{16}\text{O}_3/^{18}\text{OCS}/\text{Ar}$  and observed the CO product with only  $\text{C}^{16}\text{O}$  and  $\text{C}^{18}\text{O}$ , respectively, indicating that the oxygen atom of CO comes from OCS, not from  $\text{O}(^1\text{D})$ . In contrast, Jaeger et al. performed similar matrix experiments and reported that reaction 5 is major; some S atom product is further oxidized to  $\text{SO}_2$ ,  $\text{SO}_3$ , and  $\text{SO}_4$ .<sup>16</sup> Their  $^{18}\text{O}_3/^{16}\text{OCS}$  experiments lead to the formation of  $\text{S}^{18}\text{O}_2$  and  $^{16}\text{O}^{18}\text{O}$ , supporting the proposed mechanism. To investigate the gaseous reaction of  $\text{O}(^1\text{D}) + \text{OCS}$ , Shortridge and Lin applied resonance absorption of CO laser emission to determine the vibrational population of CO produced upon UV ( $\lambda > 215$  nm) photolysis of mixtures of  $\text{O}_3/\text{OCS}/\text{SF}_6$ ; CO ( $v \leq 9$ ) with vibrational temperature of 3300 K, corresponding to 4% of the available reaction energy, was reported.<sup>8</sup>

Froese et al. calculated a single-point energy with full fourth-order Møller–Plesset perturbation theory (MP4SDTQ) on structures optimized with second-order Møller–Plesset (MP2) for the singlet and triplet PES of the  $\text{SCO}_2$  system.<sup>17</sup> They found that the singlet complexes are more stable than the triplet complexes and proposed that reaction 1 might proceed on the singlet surface; multiple intersystem crossings are required to connect ground-state reactants to products because both have triplet multiplicity.

No report regarding the quenching by OCS of  $\text{O}(^1\text{D})$  to  $\text{O}(^3\text{P})$ , reaction 3, is available. For the reaction  $\text{O}(^3\text{P}) + \text{OCS}$ , no experimental information is available on the reaction channel for the production of  $\text{CO}_2 + \text{S}$ , and the reported internal distributions of CO have large uncertainties. For the reaction  $\text{O}(^1\text{D}) + \text{OCS}$ , the dynamics of the channel  $\text{CO}_2 + \text{S}$  are also unreported. Here we present observations of the time-resolved IR emission spectra of product molecules CO and  $\text{CO}_2$  of the reactions  $\text{O}(^1\text{D}, ^3\text{P}) + \text{OCS}$ . The nascent distributions of internal states of these product molecules are derived and compared with those calculated assuming a statistical partitioning of the reaction energy into internal degrees of freedom of the product molecules. Furthermore, to understand the reaction mechanisms further, we performed high-level quantum chemical calculations on this system including the singlet–triplet crossing points with the CCSD(T)/6-311+G(3df)/B3LYP/6-311+G(3df) methods.

## Experiments

The apparatus employed to obtain step-scan time-resolved Fourier transform spectra (TR-FTS) has been previously described;<sup>18–20</sup> only a summary is given here. A telescope mildly focused the photolysis beam from a KrF laser (248 nm, 23 Hz,  $\sim 50$  mJ) to an area  $\sim 9 \times 10 \text{ mm}^2$  at the reaction center to yield a fluence of  $\sim 50 \text{ mJ cm}^{-2}$ ; this laser beam decomposes  $\text{O}_3$  to form  $\text{O}(^1\text{D})$ . For the reaction  $\text{O}(^3\text{P}) + \text{OCS}$ , the KrF laser was replaced by an ArF laser (193 nm, 23 Hz,  $\sim 20$  mJ) that decomposes  $\text{SO}_2$  to produce  $\text{O}(^3\text{P})$ ; the laser beam was focused to an area  $\sim 4 \times 8 \text{ mm}^2$  at the reaction center to yield a fluence

of  $\sim 67 \text{ mJ cm}^{-2}$ . The transient signal from an InSb detector equipped with a preamplifier (Kolmar Technologies, rise time  $0.34 \mu\text{s}$  and responsivity  $3.2 \times 10^6 \text{ VW}^{-1}$ ) was further amplified with a factor of 5–50 (Stanford Research Systems, model 560, bandwidth 1 MHz) before being digitized with an internal data acquisition board (12-bit) at 25 ns resolution. Data were typically averaged over 60 laser pulses at each scan step; 497 scan steps were performed to yield an interferogram resulting in spectra of resolution  $4.0 \text{ cm}^{-1}$  for  $\text{CO}_2$  detection. For  $\text{CO}$  detection, 4881 scan steps were performed to yield spectra with a spectral range  $1800\text{--}2360 \text{ cm}^{-1}$  at resolution of  $0.3 \text{ cm}^{-1}$ . The temporal response function of the instrument was determined with a pulsed IR laser beam, as described previously.<sup>21</sup> The spectral response function was calibrated using a blackbody radiation source.

For experiments on  $\text{O}(^3\text{P}) + \text{OCS}$ , approximately 30% of  $\text{SO}_2$  was dissociated upon irradiation at 193 nm on the basis of the reported absorption cross section of  $3.7 \times 10^{-18} \text{ cm}^2 \text{ molecule}^{-1}$  for  $\text{SO}_2$  at 193 nm.<sup>22</sup> Partial pressures were:  $P_{\text{SO}_2} = 0.080$  to  $0.090$  Torr,  $P_{\text{OCS}} = 0.090$  to  $0.100$  Torr, and  $P_{\text{Ar}} = 0$  to  $1$  Torr. Flow rates were  $F_{\text{SO}_2} = 2.0$  to  $2.3$  sccm,  $F_{\text{OCS}} = 2.0$  to  $2.5$  sccm, and  $F_{\text{Ar}} = 0$  to  $25$  sccm; sccm denotes  $1 \text{ cm}^3 \text{ min}^{-1}$  under standard conditions (273.15 K and 760 Torr). The absorption cross section of  $\text{OCS}$  at 193 nm is  $1.8 \times 10^{-20} \text{ cm}^2 \text{ molecule}^{-1}$ .<sup>23</sup>

For experiments on  $\text{O}(^1\text{D}) + \text{OCS}$ , ozone ( $\text{O}_3$ ) and  $\text{OCS}$  were injected separately into the reaction chamber. To decrease the collision quenching of  $\text{CO}_2$  and  $\text{CO}$ , a minimal pressure yielding acceptable signals was used:  $P_{\text{O}_3} = 0.016$  to  $0.069$  Torr,  $P_{\text{OCS}} = 0.018$  to  $0.087$  Torr, and  $P_{\text{Ar}} = 0$  to  $1.5$  Torr. Flow rates were  $F_{\text{O}_3} = 1.0$  to  $2.4$  sccm,  $F_{\text{OCS}} = 0.6$  to  $3.0$  sccm, and  $F_{\text{Ar}} = 0$  to  $70.0$  sccm. Approximately 60% of  $\text{O}_3$  was dissociated upon irradiation at 248 nm on the basis of the reported absorption cross section of  $1.15 \times 10^{-17} \text{ cm}^2 \text{ molecule}^{-1}$  for  $\text{O}_3$  at 248 nm.<sup>24</sup> The depletion of  $\text{O}_3$  in the flowing system after each laser pulse was modest, as was confirmed by the negligible variation of the signal intensity when we varied the repetition rate of the photolysis laser from 20 to 30 Hz. To minimize quenching of the produced  $\text{O}(^1\text{D})$  to  $\text{O}(^3\text{P})$  by collisions with  $\text{O}_3$ , of which the rate coefficient is comparable to that with  $\text{OCS}$ , the molar fraction of  $\text{O}_3$  in the  $\text{OCS} + \text{O}_3$  mixture was maintained at less than 30%, except for experiments to detect product  $\text{CO}$  in which the fraction of  $\text{O}_3$  was  $\sim 60\%$ .

$\text{SO}_2$  (AGA Gas, 99.98%) and  $\text{Ar}$  (Linde Gas, 99.995%) were employed without further purification, and  $\text{OCS}$  (Linde, 98%) was purified upon being passed through a trap filled with molecule sieve 3A (Ridel-deH n). Impurities such as  $\text{CO}_2$  and  $\text{CS}_2$  were monitored with IR absorption in a 10 cm cell filled with  $\text{OCS}$  at 8 Torr; and no absorption other than  $\text{OCS}$  was observed.  $\text{O}_3$  was produced from  $\text{O}_2$  (Scott Specialty Gases, 99.995%) with an ozone generator (Polymetrics, model T-408) and stored over silica gel at 196 K. The partial pressure of  $\text{O}_3$  was determined from the absorption of Hg emission at 254 nm in a cell of length 7.0 cm; the absorption cross section of  $\text{O}_3$  at 254 nm was taken to be  $1.15 \times 10^{-17} \text{ cm}^2$ .<sup>25</sup>

## Computational Methods

Geometries of reactants, products, intermediates, and transition states on the PESs of the  $\text{O}(^3\text{P}, ^1\text{D}) + \text{OCS}$  reaction were optimized with B3LYP/6-311+G(3df) density functional theory (DFT).<sup>26</sup> The vibrational wavenumbers were calculated at this level to characterize local minima and transition state and corrections of zero-point energy (ZPE). To obtain reliable energies and rate coefficient predictions, we calculated single-

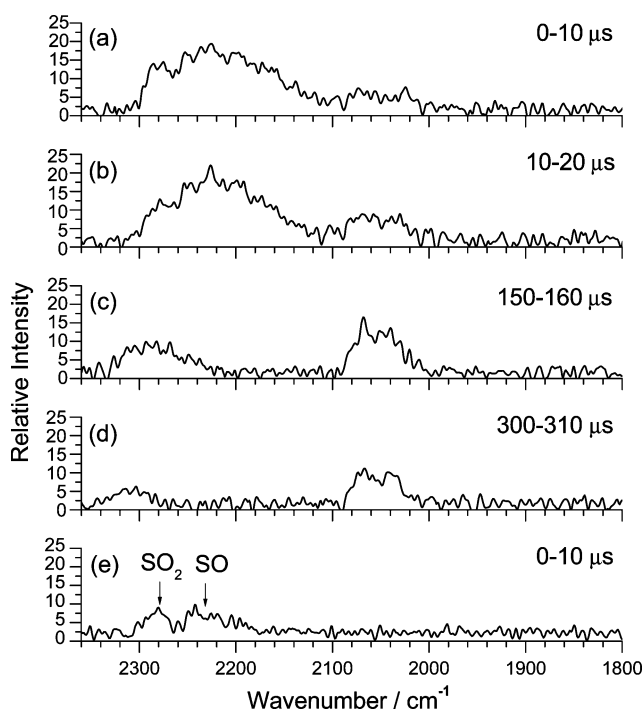


**Figure 1.** Time-resolved emission spectra observed upon irradiation at 193 nm of a mixture containing  $\text{SO}_2$  (0.080 Torr) and  $\text{OCS}$  (0.100 Torr). Each spectrum is obtained upon integration at  $10 \mu\text{s}$  intervals with delays of (a) 0, (b) 10, (c) 150, and (d) 300  $\mu\text{s}$ . (e) Emission spectrum of  $\text{SO}_2$  (0.080 Torr) irradiated at 193 nm. Spectral resolution is  $4 \text{ cm}^{-1}$ , and the fluence of the photolysis laser is  $\sim 43 \text{ mJ cm}^{-2}$ .

point energies at level CCSD(T)/6-311+G(3df) on the basis of the structures at the B3LYP/6-311+G(3df), expressed as CCSD(T)/6-311+G(3df)//B3LYP/6-311+G(3df). Calculations of the intrinsic reaction coordinate (IRC)<sup>26</sup> were performed to connect each transition state with designated reactants and products. All calculations of electronic structure were performed with the Gaussian 03 program.<sup>27</sup> For points of the surface intersection (MSX), their geometry was located using the state-averaged complete active space self-consistent field (CASSCF)<sup>28</sup> method with the 6-311+G(3df) basis set. The default value, six electrons in six active orbitals, in the Gaussian program was used for the CASSCF calculations; the active space is defined assuming that the electrons come from the highest occupied orbitals in the initially guessed determinant and that the remaining orbitals required for the active space come from the lowest virtual orbitals of the initial guess. The vibrational wave numbers of the intersection point are calculated at the B3LYP/6-311+G(3df) level on the singlet surface. The number of imaginary frequencies (NIMG) with NIMG = 1 was obtained, indicating that the MSX has transition-state characteristics. An MSX between singlet and triplet PES is treated as a transition state for the adiabatic reaction in our estimation of the rate coefficient for the ground-state reaction to which we later allude.

## Results and Discussion

**A. Infrared Emission from the  $\text{O}(^3\text{P}) + \text{OCS}$  System.** Observed time-resolved IR emission spectra from the reaction  $\text{O}(^3\text{P}) + \text{OCS}$ , in which  $\text{O}(^3\text{P})$  was produced upon photodissociation of  $\text{SO}_2$  at 193 nm, are shown in Figure 1. Two weak emission bands are identified in the region  $1800\text{--}2360 \text{ cm}^{-1}$ . The broadband with maximum intensity near  $2200 \text{ cm}^{-1}$  and a full width at half-maximum (fwhm) of  $130 \text{ cm}^{-1}$





each vibrational transition is compared with experimental data in trace c of Figure 2. The thick line indicates the observed spectrum, and the thin line indicates a spectrum simulated with a rotational temperature of 500 K; the shaded area represents the uncertainty limits of  $\pm 200$  K. The experimental and simulated spectra agree satisfactorily. The band shape is mainly determined by the available energy  $E^*$ ; the rotational energy has only a limited effect on the band shape and has little effect on the position of the maximal intensity.

The rotational distribution might be determined inaccurately partially because the band shape is insensitive to rotational temperature and partially because the calculated vibrational term values and their transition frequencies are given as a zeroth-order approximation and the rotational parameters of the highly excited states are unknown. Because of the extremely dense vibrational transition lines, the band shape given as convoluted rotational envelopes for each vibrational transition might not depend significantly on the positions of vibrational transitions.

In these experiments,  $O(^3P)$  is produced upon photodissociation of  $SO_2$  at 193 nm. The dissociation energy of  $SO_2$  to form  $SO(X^3\Sigma^-) + O(^3P)$  is  $45\,400\text{ cm}^{-1}$ , and the excess energy given to  $SO$  and  $O$  is thus  $6300\text{ cm}^{-1}$ . The internal energy distribution of  $SO^{33-36}$  and the velocity distribution of  $SO^{37,38}$  and  $O^{39,40}$  upon  $SO_2$  photodissociation have been reported. It is a general consensus that the vibrational population of the  $SO(v=2)$  level is largest and the populations for  $v \geq 4$  are negligible upon photolysis of  $SO_2$  at 193 nm. We use the kinetic energy determined by Brouard et al. as a representative value.<sup>40</sup> The average value of the space-fixed kinetic energy of  $O$  atom is  $32 \pm 11\text{ kJ mol}^{-1}$ , corresponding to  $2675\text{ cm}^{-1}$ . In a collision of  $O$  atom with  $OCS$ , the center-of-mass kinetic energy becomes  $(32 \pm 11) \times [60/(16 + 60)] + 3.7 \times [16/(16 + 60)] = 26 \pm 9\text{ kJ mol}^{-1}$  ( $2170 \pm 750\text{ cm}^{-1}$ ), in which 16 and 60 amu are the atomic and molecular masses of  $O$  and  $OCS$ , respectively, and  $3.7\text{ kJ mol}^{-1}$  is the thermal kinetic energy of  $OCS$  at room temperature. According to reaction 2, the available energy in our experiment is  $E^* = 227 + 26 = 253\text{ kJ mol}^{-1}$ , corresponding to  $21\,150\text{ cm}^{-1}$ . If a statistical distribution in the spin-orbit states is assumed for  $O(^3P)$  and  $S(^3P)$ , then the above value of  $E^*$  is corrected to be  $21\,150 + 78 - 196 = 21\,032\text{ cm}^{-1}$ , in which  $78\text{ cm}^{-1}$  is the statistical spin-orbit energy of  $O(^3P_{0,1,2})$  and  $196\text{ cm}^{-1}$  is that of  $S(^3P_{0,1,2})$ . The energies of  $S(^3P_J)$  in the  $J = 2, 1$ , and  $0$  states are  $0, 396$ , and  $574\text{ cm}^{-1}$ , respectively; the statistically distributed  $S$  atom has an average energy of  $196\text{ cm}^{-1}$  above the ground  $J = 2$  state.

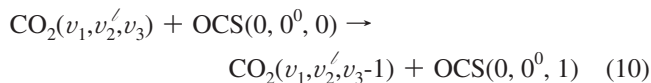
The vibrational distribution that yields the best fit with the observed band shape is obtained on the statistical partitioning of energy  $E^* = 18\,000 \pm 1000\text{ cm}^{-1}$ , which is 86% of the available energy. This result is similar to the case of  $O(^1D) + CO_2 \rightarrow O(^3P) + CO_2$  in which the best fit of  $\nu_3$  emission band is obtained upon statistical partitioning of  $E^* = 13\,000 \pm 500\text{ cm}^{-1}$  that is 81% of the available energy. Because the vibrational energy of product  $CO_2$  in both reactions is near the statistical partitioning of the reaction energy, the reaction likely proceeds through a relatively long-lived complex  $O_2CS$  or  $CO_3$  in which the internal energy is nearly completely randomized.

According to the distribution of vibrational states derived from vibrational transitions depicted in Figure 2a, the observed average vibrational energy of product  $CO_2$  is  $10\,280\text{ cm}^{-1}$ , which corresponds to  $\sim 49\%$  of the available energy, similar to the value of 44% for the reaction  $O(^1D) + CO_2$ . The roughly estimated rotational temperature of  $500 \pm 200\text{ K}$  for  $CO_2$ ,

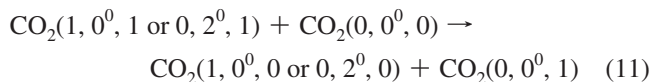
corresponding to  $<2\%$  of the available energy, indicates that  $CO_2$  has little rotational excitation, similar to the case of  $O(^1D) + CO_2$ .<sup>14</sup>

**2. OCS Emission.** The band that appears near  $2060\text{ cm}^{-1}$  (Figure 1) was assigned to the emission of  $OCS$  in the  $CO$  stretching ( $\nu_3$ ) mode. Because the position of this band does not change during observation, the emission is not from highly vibrationally excited states, as in the case of  $CO_2$  emission; the emission is thus due to the vibrational transition of  $\nu_3 = 1 \rightarrow 0$ . As shown in Figure 1, the intensity of this band increases in the initial stage with a rate similar to that of  $CO_2$ , indicating that the source of the vibrational excitation of  $OCS$  is common to the formation of  $CO_2$ . In the later stage, the band center of the  $CO_2$  emission shifts toward a larger wavenumber, and its intensity decreases with a time constant of  $\sim 75\text{ }\mu\text{s}$ , whereas the intensity of the  $OCS$  band increases toward a stationary value.

The fundamental vibrational wavenumbers for  $\nu_3$  of  $CO_2$  and  $OCS$  differ by  $287\text{ cm}^{-1}$ ; the collision probability of the  $V-V$  energy transfer between  $OCS(\nu_3 = 1)$  and  $CO_2(\nu_3 = 1)$  is consequently on the order of  $10^{-4}$  because of a large difference in transition energies.<sup>41</sup> For highly vibrationally excited  $CO_2$ , the anharmonic coupling between  $\nu_3$  and  $\nu_1/\nu_2$  modes decreases; however, the energy separation between  $\nu_3$  and  $\nu_3 - 1$  levels of  $CO_2$  becomes resonant with the energy separation between the  $(0, 0^0, 0)$  and  $(0, 0^0, 1)$  levels of  $OCS$



so that efficient  $V-V$  energy transfer occurs. Finzi and Moore reported intermolecular  $V-V$  energy transfer of this type;<sup>42</sup> the rate coefficients for the  $V-V$  energy transfer



were determined to be  $1.2 \times 10^{-10}\text{ cm}^3\text{ molecule}^{-1}\text{ s}^{-1}$ , near the gas kinetic rate coefficient for collision. The observed weak emission of  $OCS$  hence comes from  $V-V$  energy transfer from highly vibrationally excited  $CO_2$  to  $OCS(0, 0^0, 1)$ . This phenomenon was observed more clearly in the reaction of  $O(^1D) + OCS$ ; the kinetic analysis will hence be given in Section C2.

**B. Infrared Emission from the  $O(^3P) + OCS + Ar$  System.** Figure 3 shows how the emission band observed in the period  $0-10\text{ }\mu\text{s}$  varies with the partial pressure of  $Ar$  buffer gas in the reaction  $O(^3P) + OCS$ . The intensity of  $CO_2$  emission decreased to less than half when 100 mTorr of  $Ar$  was added to a mixture of  $SO_2$  (80 mTorr) and  $OCS$  (100 mTorr) for experiments (traces a and b); it diminished to almost zero when 500 mTorr of  $Ar$  was added, as shown in trace c of Figure 3. The role of  $Ar$  is to deactivate hot atoms or molecules by collisions. The collision number of  $Ar$  atom with an excited species within  $10\text{ }\mu\text{s}$  is less than 10 in our experiments under low pressure. At greater pressures, the rates of collision increase; the translational energy might be consequently deactivated efficiently to a value smaller than the barrier for the  $O(^3P) + OCS$  reaction, resulting in a diminished yield of products.

When  $SO_2$  is irradiated at 193 nm, translationally hot  $O(^3P)$  atoms are produced to initiate their reactions with  $OCS$ , but some of them are subsequently deactivated on collisions with surrounding atoms and molecules. When all  $O$  atoms are

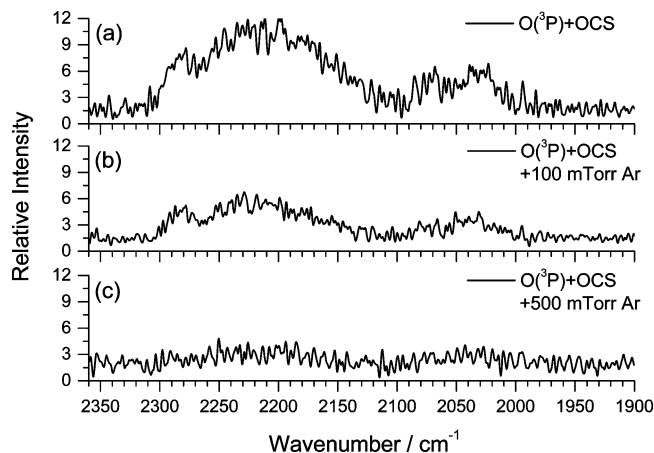


**Figure 3.** Emission spectra observed 0–10  $\mu\text{s}$  upon irradiation at 193 nm of a mixture containing  $\text{SO}_2$  (0.080 Torr),  $\text{OCS}$  (0.10 Torr), and Ar. The partial pressure of Ar varies from (a) 0, (b) 0.10, and (c) 0.50 Torr. Spectral resolution is 2  $\text{cm}^{-1}$ , and the fluence of the photolysis laser is  $\sim 70 \text{ mJ cm}^{-2}$ .

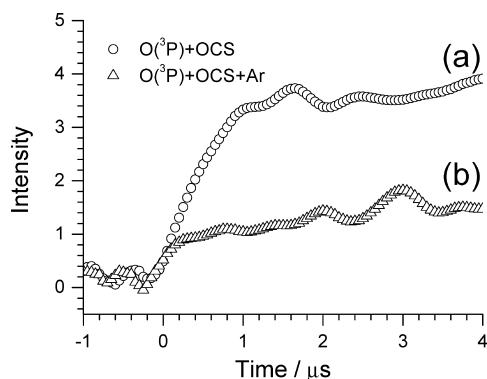


**Figure 4.** Temporal profiles of the emission intensities of  $\text{CO}_2$  upon irradiation of a flowing mixture of (a)  $\text{SO}_2$  (0.088 Torr) +  $\text{OCS}$  (0.095 Torr) and (b)  $\text{SO}_2$  (0.088 Torr) +  $\text{OCS}$  (0.095 Torr) + Ar (0.092 Torr) with an excimer laser at 193 nm with a fluence of  $73 \text{ mJ cm}^{-2}$ .

quenched to have kinetic energy less than the threshold, the reaction stops. Figure 4 shows temporal profiles of integrated intensity of  $\text{CO}_2$  emission for two irradiated flowing mixtures; trace a is from a mixture containing 0.088 Torr of  $\text{SO}_2$  and 0.095 Torr of  $\text{OCS}$ , and trace b is from a similar mixture but with 0.092 Torr of Ar added. In trace a, the intensity of  $\text{CO}_2$  reaches a steady value near 0.8  $\mu\text{s}$ , whereas in trace b, this value decreases to 0.2  $\mu\text{s}$  and the intensity decreases to  $\sim 40\%$  of that of part a.

According to Abe et al.,<sup>43</sup> the average kinetic energy in a laboratory frame of translationally hot  $\text{O}(^3\text{P})$  atoms produced from the photodissociation of  $\text{SO}_2$  in a buffer gas Q is deactivated within a few collisions in the initial stage according to the approximate equation

$$\frac{\langle E^{\text{LAB}}(t) \rangle - \langle E_{\text{eq}} \rangle}{\langle E^{\text{LAB}}(t=0) \rangle - \langle E_{\text{eq}} \rangle} = \exp(-k_{\text{q}}[Q]t) \quad (12)$$

in which  $\langle E^{\text{LAB}}(t) \rangle$  and  $\langle E_{\text{eq}} \rangle$  are the average kinetic energies of O atoms at time  $t$  and at equilibrium, respectively,  $k_{\text{q}}$  is the rate coefficient, and  $[Q]$  is the concentration of the quencher. In our reaction system containing  $\text{SO}_2$ ,  $\text{SO}$ , and  $\text{OCS}$ , the rate coefficients for deactivation of O atoms by these species are unknown. We hence used  $k_{\text{q}}(\text{Ar}) = k_{\text{q}}(\text{Kr}) = 1.5 \times 10^{-10} \text{ cm}^3$

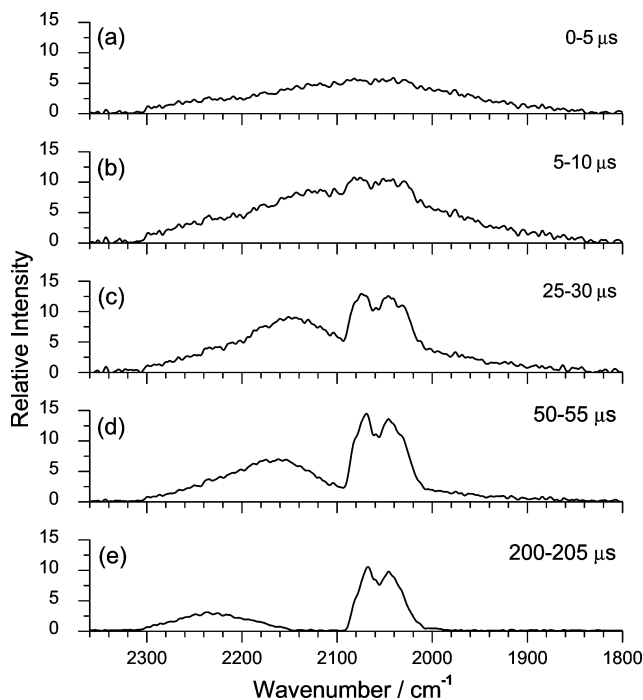


**Figure 5.** Time-resolved emission spectra observed upon irradiation at 248 nm of a mixture containing  $\text{O}_3$  (0.026 Torr) and  $\text{OCS}$  (0.021 Torr). Each spectrum is obtained upon integration at 5  $\mu\text{s}$  intervals with delays of (a) 0, (b) 5, (c) 25, (d) 50, and (e) 200  $\mu\text{s}$ . Spectral resolution is 4  $\text{cm}^{-1}$ , and the fluence of the laser is  $\sim 80 \text{ mJ cm}^{-2}$ .

molecule<sup>-1</sup> s<sup>-1</sup> and assume that these coefficients for  $\text{SO}_2$ ,  $\text{SO}$ , and  $\text{OCS}$  are the same as  $k_{\text{q}}(\text{CO}_2) = 3 \times 10^{-10} \text{ cm}^3 \text{ molecule}^{-1} \text{ s}^{-1}$  and that every collision of translationally hot  $\text{O}(^3\text{P})$  with  $\text{OCS}$  leads to the reaction. The initial average kinetic energy of  $\text{O}(^3\text{P})$  produced upon photodissociation of  $\text{SO}_2$  at 193 nm is  $32 \pm 11 \text{ kJ mol}^{-1}$  in the laboratory frame. Assuming that the kinetic energy is deactivated according to eq 12, we estimated the average kinetic energy of  $\text{O}(^3\text{P})$  in the center-of-mass frame, which was  $26 \pm 9 \text{ kJ mol}^{-1}$  at  $t = 0$  to be  $18 \pm 6 \text{ kJ mol}^{-1}$  at 0.8  $\mu\text{s}$  for the gaseous mixture employed in part a and  $22 \pm 7 \text{ kJ mol}^{-1}$  at 0.2  $\mu\text{s}$  for the mixture b. The upper limit of these estimated values of 24–29  $\text{kJ mol}^{-1}$  might correspond to an approximate value of the barrier height for the reaction channel to form  $\text{CO}_2$  because under such conditions, no further increase in  $\text{CO}_2$  emission was observed; the estimates have large errors because of unknown rate coefficients of deactivation and uncertain kinetic energy distributions of  $\text{O}(^3\text{P})$  during quenching.

We thus conclude that the reaction of  $\text{O}(^3\text{P}) + \text{OCS}$  proceeds only with translationally hot  $\text{O}(^3\text{P})$  that has sufficient energy to overcome the barrier of the reaction. When more Ar is added to the system, the fraction of  $\text{O}(^3\text{P})$  that has sufficient energy to overcome the barrier decreases, and hence the yield of  $\text{CO}_2$  decreases.

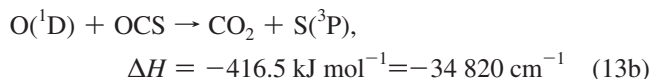
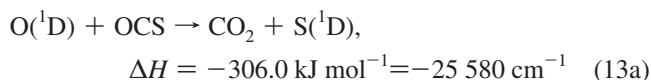
#### C. Infrared Emission from the $\text{O}(^1\text{D}) + \text{OCS}$ System.

Figure 5 shows time-resolved emission spectra in the 1800–2360  $\text{cm}^{-1}$  region observed from a  $\text{O}_3/\text{OCS}$  mixture irradiated at 248 nm. In the initial stage, only one broadband with maximal intensity near 2070  $\text{cm}^{-1}$  and a fwhm of 220  $\text{cm}^{-1}$  was observed (trace a). We assign the broadband as the  $\Delta\nu_3 = -1$  emission of internally excited  $\text{CO}_2$ , which is similar to that observed in the  $\text{O}(^1\text{D}) + \text{CO}_2$  (ref 14) and  $\text{O}(^3\text{P}) + \text{OCS}$  systems. Compared with the emission spectra of  $\text{CO}_2$  shown in Figure 1 of ref 14 and Figure 1 of this article, the band position is located at a much smaller wavenumber, indicating much more extensive vibrational excitation of  $\text{CO}_2$ .



The maximum of the CO<sub>2</sub> band shifts toward greater wavenumbers, and the width of the band decreases at a later period, as shown in traces b–e of Figure 5. In the spectrum at a reaction time of 5–10 μs (trace b), a new band centered near 2055 cm<sup>-1</sup> appears, and its intensity subsequently increases. This band consists of P and R branches and is readily assigned to the  $\nu_3 = 1 \rightarrow 0$  transition of OCS. The intensity of this band increases to attain its maximum near 80 μs. In contrast, the intensity of the CO<sub>2</sub> band diminishes continuously and more rapidly.

**1. Emission of CO<sub>2</sub>.** The following two reactions are responsible for the production of vibrationally excited CO<sub>2</sub>



in which values of  $\Delta H$  at 0 K are taken from the JANAF table.<sup>44</sup> In reaction 13b, the distribution of spin–orbit states of the product S atom is expected to be statistical because the mechanism is likely similar to the reaction  $\text{O}(^1\text{D}) + \text{CO}_2$  in which the distribution in respective  $J$  states of  $\text{O}(^3\text{P}_j)$  was reported to be nearly statistical.<sup>45</sup>

If the reaction  $\text{O}(^1\text{D}) + \text{OCS}$  proceeds through a long-lived intermediate O<sub>2</sub>CS, similar to CO<sub>3</sub> in  $\text{O}(^1\text{D}) + \text{CO}_2$ ,<sup>14</sup> then the electronic energy of  $\text{O}(^1\text{D})$  is likely partitioned statistically among the degrees of freedom of the product molecules. The distribution among the excited vibrational states of CO<sub>2</sub> was calculated under an assumption of statistical partitioning of the energy  $E_{13a}^*$  and  $E_{13b}^*$  released in reactions 13a and 13b, respectively. The initial average kinetic energy of  $\text{O}(^1\text{D})$  that is produced upon photolysis of O<sub>3</sub> at 248 nm was determined to be 36 kJ mol<sup>-1</sup>, corresponding to 3010 cm<sup>-1</sup>.<sup>46</sup> These hot  $\text{O}(^1\text{D})$  atoms are, however, rapidly deactivated with collisions with surrounding molecules. The rate coefficient for deactivation by collisions with O<sub>2</sub> is  $1.5 \times 10^{-10} \text{ cm}^3 \text{ molecule}^{-1} \text{ s}^{-1}$ .<sup>47</sup> If we assume the same rate coefficient for the present system of reaction mixtures of O<sub>2</sub> and OCS, then the average space-fixed kinetic energy of  $\text{O}(^1\text{D})$  during the reaction interval of 2 μs upon photolysis of O<sub>3</sub> is hence estimated to be 25.0 kJ mol<sup>-1</sup>, corresponding to 2341 cm<sup>-1</sup>. In the center-of-mass coordinate of the  $\text{O}(^1\text{D}) + \text{OCS}$  collision, the kinetic energy is  $25.0 \times (60/76) + 3.7 \times (16/76) = 20.5 \text{ kJ mol}^{-1}$  (or 1715 cm<sup>-1</sup>), in which 3.7 kJ mol<sup>-1</sup> represents the thermal kinetic energy of OCS. The available energies to be partitioned to the products in reactions 13a and 13b are thus  $E_{13a}^* = 25\,580 + 1715 = 27\,295 \text{ cm}^{-1}$  and  $E_{13b}^* = 34\,820 + 1715 - 196 = 36\,339 \text{ cm}^{-1}$ , respectively; the value 196 cm<sup>-1</sup> is the average spin–orbit state energy of the product S atom. If  $\text{O}(^1\text{D})$  atoms are completely thermalized, then  $E_{13a}^* = 25\,580 + 310 = 25\,890 \text{ cm}^{-1}$  and  $E_{13b}^* = 34\,820 + 310 - 196 = 34\,934 \text{ cm}^{-1}$ .

Similar to the procedures described for the reaction  $\text{O}(^3\text{P}) + \text{OCS}$  in Section A, the best fit spectrum was obtained with  $E^* = 30\,000 \pm 500 \text{ cm}^{-1}$ , as shown in Figure 6. Trace a is a stick diagram of  $\Delta \nu_3 = -1$  transitions calculated with the  $\nu_1/\nu_2$  polyad approximation,<sup>14</sup> and trace b represents the same distribution convoluted with fwhm = 4 cm<sup>-1</sup>; the latter provides a practical comparison of vibrational distributions with experimental data. The final spectrum simulated with rotational distribution incorporated into each vibrational transition is

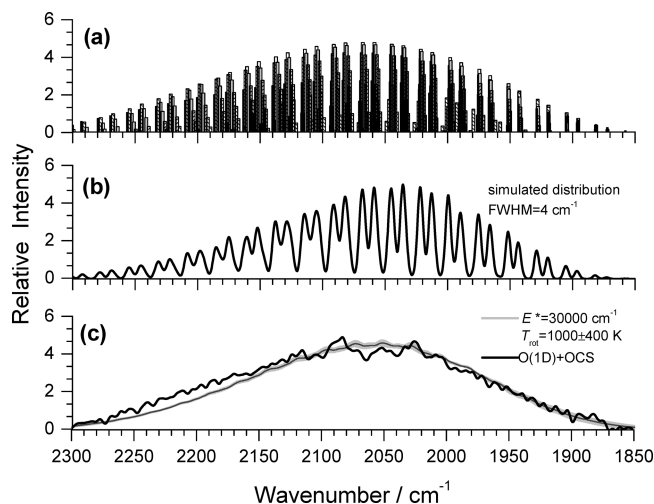


**Figure 6.** Simulation of the observed emission band of product CO<sub>2</sub> in the reaction  $\text{O}(^1\text{D}) + \text{OCS}$ . (a) Vibrational band origins from CO<sub>2</sub> excited on statistical partitioning of available energy  $E^* = 30\,000 \text{ cm}^{-1}$ , (b) calculated band contour obtained on convoluting lines in part a with Gaussian functions with fwhm of 4 cm<sup>-1</sup>, and (c) comparison of the observed spectrum (thick solid line, same as Figure 5a) with the spectrum simulated on convoluting lines in part a with rotational contours calculated for 1000 K with the PGopher program (thin solid line). The shaded area indicates uncertainties ( $\pm 400 \text{ K}$ ) in the rotational temperature.

compared with experimental data in trace c of Figure 6. The thick line indicates the observed spectrum, and the thin line indicates the simulated spectrum with a rotational temperature of 1000 K; the shaded area represents the uncertainty limits of  $\pm 400 \text{ K}$ . The experimental and simulated spectra agree satisfactorily.

This fitted value of  $E^*$  is  $\sim 85\%$  of the available energy,  $34\,934\text{--}36\,339 \text{ cm}^{-1}$ , for the triplet channel and  $\sim 113\%$  of the available energy,  $25\,890\text{--}27\,295 \text{ cm}^{-1}$ , for the singlet channel. The former fraction (86%) is similar to the corresponding values (81 and 86%, respectively) of  $\text{O}(^1\text{D}) + \text{CO}_2$  and  $\text{O}(^3\text{P}) + \text{OCS}$  in which the reactions proceed through a relatively long-lived complex so that the internal energy is nearly completely randomized. However, this fact does not imply that the contribution of the singlet channel is ruled out, although the triplet product channel is expected to be dominant. In our experiment, it is difficult to derive respective contributions of the singlet and triplet product channels to the observed emission band of CO<sub>2</sub>. If we assume that the reaction intermediate O<sub>2</sub>CS\* is long-lived so that the reaction proceeds toward the singlet and triplet product channels statistically, then the branching ratio of the two channels may be formulated as  $\sum_{\text{singlet}} N(E_v) / \sum_{\text{triplet}} N(E_v)$ , in which  $N(E_v)$  is the density of vibrational states  $E_v$  determined with statistical distribution of the available energy for each channel, as given in equation 10 of ref 14. The branching ratio thus calculated is 0.23, that is, 19% to the singlet channel and 81% to the triplet channel. A more detailed discussion on the branching between singlet and triplet channels is given in Section E2.

According to the distribution of vibrational states derived from vibrational transitions depicted in Figure 6a, the observed average vibrational energy of the product CO<sub>2</sub> is  $17\,830 \text{ cm}^{-1}$ , which corresponds to  $\sim 51\%$  of the available energy, similar to the value of 44% for the reaction  $\text{O}(^1\text{D}) + \text{CO}_2$ . The roughly estimated rotational temperature of  $1000 \pm 400 \text{ K}$  for CO<sub>2</sub>, corresponding to  $<2\%$  of the available energy, indicates that CO<sub>2</sub> has little rotational excitation, similar to the case of  $\text{O}(^1\text{D}) + \text{CO}_2$ .<sup>14</sup>



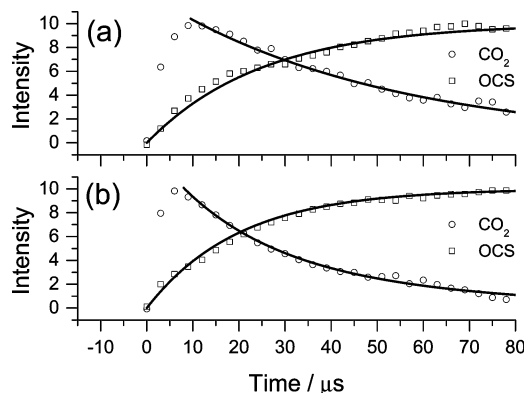


**Figure 7.** Temporal profiles of integrated emission of  $CO_2$  and  $OCS$  for two mixtures: (a)  $P_{OCS} = 0.021$ ,  $P_{O_3} = 0.026$  Torr and (b)  $P_{OCS} = 0.051$ ,  $P_{O_3} = 0.022$  Torr. The overlapping emission bands of  $CO_2$  and  $OCS$  were deconvoluted. Rate coefficients determined from the decay of  $CO_2^*$  are  $k_{VV} =$  (a)  $3 \times 10^{-11}$  and (b)  $2 \times 10^{-11}$   $cm^3$  molecule $^{-1}$  s $^{-1}$  and from the rise of  $OCS^*$  are  $k_{VV} =$  (a)  $6 \times 10^{-11}$  and (b)  $3 \times 10^{-11}$   $cm^3$  molecule $^{-1}$  s $^{-1}$ , respectively.

**2. Emission of  $OCS$ .** As shown in Figure 5, only the broad  $CO_2$  band located near  $2050$   $cm^{-1}$  appears in an early stage of the  $O(^1D) + OCS$  reaction, and an additional band assigned to  $\nu_3 = 1 \rightarrow 0$  of  $OCS$  increases in intensity  $15$   $\mu s$  after initiation of reaction, whereas the intensity of the  $CO_2$  emission diminishes, and its maximum shifts to a larger wavenumber. As discussed in Section A2, the excitation of  $OCS$  is due to V–V energy transfer from highly vibrationally excited  $CO_2$  produced from  $O(^1D) + OCS$  (reaction 10), not to quenching of  $O(^1D)$  (reaction 3); the highly excited  $CO_2$  molecules transfer their energy in the  $\nu_3$  mode to  $OCS$  as a nearly resonant process.

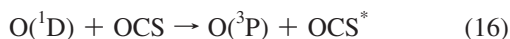
Figure 7 shows temporal profiles of the integrated emission intensities of  $CO_2$  and  $OCS$  at two partial pressures of  $OCS$ . With a simple model of vibrational energy transfer, the rise of  $OCS$  and decay of  $CO_2$  might be described with

$$[OCS^*] = [CO_2^*]_0 [1 - \exp(-k_{VV}[OCS]t)] \quad (14)$$

$$[CO_2^*] = [CO_2^*]_0 \exp(-k_{VV}[OCS]t) \quad (15)$$

in which  $k_{VV}$  is the bimolecular rate coefficient for V–V energy transfer. The data in Figure 7 yield  $k_{VV} = (3.5 \pm 1.5) \times 10^{-11}$   $cm^3$  molecule $^{-1}$  s $^{-1}$ ; the error limit represents only the uncertainties in fitted values of  $k_{VV}$  using this model. This value provides a qualitative description of the energy transfer because the present kinetic model involves several assumptions including the instant formation of excited  $CO_2$  from reaction  $O(^1D) + OCS$ , no dependence of the V–V rate coefficient on the extent of the excitation of  $CO_2$ , and the neglecting of the reverse V–V transfer from  $OCS$  to  $CO_2$ . The large value of  $k_{VV}$  indicates that the emission band of  $CO_2$  overlaps well with the  $OCS$  fundamental absorption so that the nearly resonant V–V transfer is efficient. In contrast, for  $O(^3P) + OCS$ , the extent of the overlap is smaller because less highly internally excited  $CO_2$  is produced.

An important finding is that the collision probability of the reaction involving the transfer of electronic to vibrational (E–V) energy

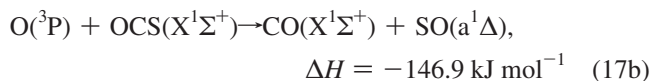
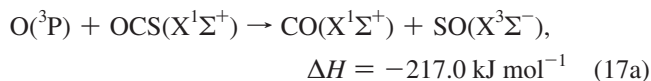


is small, as seen from the negligible emission of  $OCS$  in the initial stage of reaction. This observation is quite different from that for the reaction of  $O(^1D) + CO_2$ . Perri et al.<sup>48,49</sup> showed clearly from the  $^{18}O(^1D) + ^{44}CO_2$  isotope exchange reaction in a crossed beam that only two exit channels are possible for the complex  $CO_3^*$ : one is the reverse reaction of  $O(^1D) + CO_2$ , and the other is the crossing to the triplet PES to form  $O(^3P)$  and internally excited  $CO_2$ . In contrast, the collision complex of  $O_2CS^*$  might dissociate via several channels on both singlet and triplet PESs, of which the products are located in energy regions much lower than  $O(^3P) + OCS$ ; the density of states in the  $O(^3P) + OCS$  channel is thus negligibly small compared with those of the reaction channels.

**3. Emission of  $CO$ .** When the emission was recorded with greater spectral resolution, weak emission lines were identified in the region  $2000$ – $2230$   $cm^{-1}$  overlapping the broad  $CO_2$  emission band, as shown in Figure 8. These emission lines are due to internally excited  $CO$  that was produced in the reaction  $O(^1D) + OCS$  (reaction 4). The respective lines are assigned as the  $P(J)$  and  $R(J)$  rotational lines of the  $\nu \rightarrow \nu - 1$  vibrational transition, as marked in the upper part of the Figure. The assignments and the population analysis of these vibration–rotational transition lines of  $CO$  are described in detail elsewhere.<sup>50,51</sup> Following this analysis of  $CO$ , the rotational distributions of  $CO$  in its respective vibrational states and the vibrational distribution are presented in Figure 9a,b, respectively. The rotational distributions are Boltzmann-like, and the rotational temperatures range from  $520$  to  $810$  K for  $\nu = 3$  to  $1$ ; the average rotational energy is  $5.4 \pm 0.5$   $kJ$  mol $^{-1}$ , only  $2.5\%$  of the released energy in the triplet channel and  $3.8\%$  in the singlet channel. Similarly, the vibrational distribution is also Boltzmann-like; we hence estimate the population of  $CO(\nu = 0)$  by extrapolation, shown as an open circle in Figure 9b. The vibrational temperature is  $5700 \pm 260$  K, and the average vibrational energy is  $36 \pm 2$   $kJ$  mol $^{-1}$ , corresponding to  $\sim 17\%$  of the released energy in the triplet channel and  $\sim 26\%$  in the singlet channel. The vibrational energy is greater than the value corresponding to  $3300$  K reported by Shortridge and Lin.<sup>8</sup>

**D. Reaction Mechanism and Calculated Potential Energies. 1. Geometries and Energies.** The geometries of the reactants, products, intermediates (LM), and transition states (TS) involved in the singlet and triplet reactions, optimized with the B3LYP/6-311+G(3df) method, are shown in Figure 10. Vibrational wavenumbers and rotational constants for the reactants, intermediates, transition states, crossing points (MSX), and products of the  $O(^1D, ^3P) + OCS$  reaction computed with the B3LYP/6-311+G(3df) method are listed in Table 1. The energy diagrams for singlet and triplet surfaces calculated at the CCSD(T)/6-311+G(3df)//B3LYP/6-311+G(3df) level are presented in Figure 11.

For the formation of  $CO(X^1\Sigma^-) + SO(X^3\Sigma^-)$



the predicted enthalpies of reaction for reaction 17a is  $-203.3$   $kJ$  mol $^{-1}$ ,  $6.3\%$  less exothermic than the experimental value of  $-217.0$   $kJ$  mol $^{-1}$ ; the experimental values are obtained from JANAF thermochemical tables,<sup>44</sup> except for an updated value

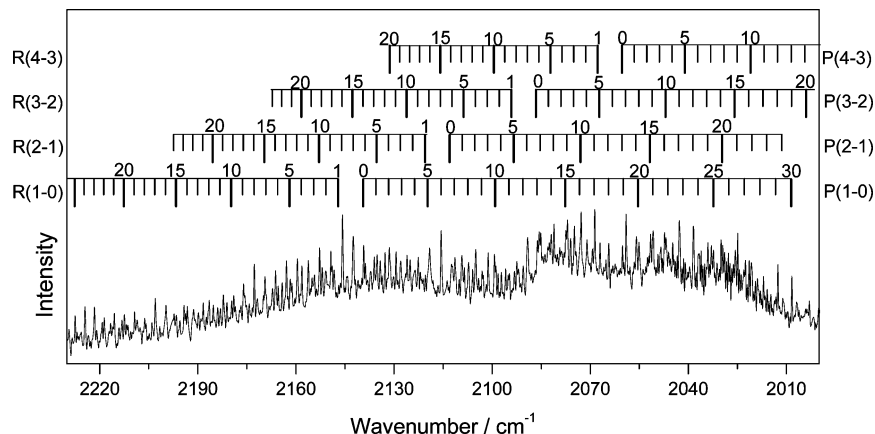
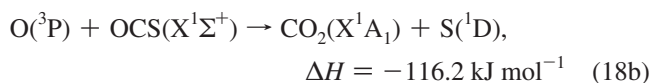
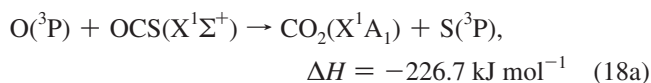


**Figure 8.** Partial emission spectrum of CO observed from the reaction  $\text{O}(^1\text{D}) + \text{OCS}$ . Partial pressures of  $\text{O}_3$  and  $\text{OCS}$  are 0.078 and 0.052 Torr, respectively. Spectral resolution is  $0.3 \text{ cm}^{-1}$ , and the fluence of the laser is  $\sim 55 \text{ mJ cm}^{-2}$ . The signals are integrated 5–10  $\mu\text{s}$  after laser irradiation.

for the energy of  $\text{SO}(a^1\Delta)$ .<sup>52</sup> For the formation of  $\text{CO}_2(X^1A_1) + \text{S}(^3\text{P})$



the predicted enthalpy of reaction is  $-227.2 \text{ kJ mol}^{-1}$ , which is also consistent with the experimental value of  $-226.7 \text{ kJ mol}^{-1}$ .

As shown in Figure 11, the triplet surfaces of reactions 17a and 18a might proceed via direct abstraction and substitution channels via TS1 and TS2, respectively, to produce  $\text{CO}(X^1\Sigma^+) + \text{SO}(X^3\Sigma^-)$  and  $\text{S}(^3\text{P}) + \text{CO}_2(X^1A_1)$ . In TS1, the distances of O–S bond formation and C–S bond breaking are 2.046 and 1.581 Å, respectively. In TS2, the distances of C–O bond formation and C–S bond breaking are 1.974 and 1.615 Å, respectively. The energy barriers are predicted to be 27.6 and 36.4  $\text{kJ mol}^{-1}$ , respectively, for these abstraction and substitution channels. The reaction  $\text{O}(^3\text{P}) + \text{OCS}(X^1\Sigma^+) \rightarrow \text{CS}(X^1\Sigma^+) + \text{O}_2(X^3\Sigma_g^-)$  is neglected because of its large barrier of 304.1  $\text{kJ mol}^{-1}$  and the large endothermicity of 181.6  $\text{kJ mol}^{-1}$ .

Two stable intermediates, LM1 and LM2, are found in the singlet surface (Figure 11). LM1 is associated with the O atom attacking the S atom of OCS, whereas LM2 is associated with the O atom attacking the C atom of OCS. The energies are calculated to be 150.1 and 190.0  $\text{kJ mol}^{-1}$  below the triplet reactants. LM1 might dissociate without a well-defined TS to excited-state products  $\text{CO}(X^1\Sigma^+) + \text{SO}(a^1\Delta)$  or isomerize to LM2 via TS3, with a barrier of 66.1  $\text{kJ mol}^{-1}$ . LM2 might dissociate without a well-defined TS to excited-state products  $\text{CO}_2(X^1A_1) + \text{S}(^1\text{D})$  or isomerize to LM1 via TS3.

We also located four crossing points (MSXi) for the singlet–triplet surfaces. The structures of MSX1 and MSX2 optimized at the CASSCF(6,6)/6-311+(3df) level are illustrated in Figure 10; their geometries are similar to those of TS1 and TS2, respectively. The energies of MSX1 and MSX2 are 14.2 and 33.4  $\text{kJ mol}^{-1}$  above  $\text{O}(^3\text{P}) + \text{OCS}(X^1\Sigma^+)$ . MSX3 and MSX4 have energies at  $-136.3$  and  $-108.3 \text{ kJ mol}^{-1}$ , slightly smaller than those of the corresponding excited-state products. The geometry of MSX4 is similar to that of LM1 except for an

increased C–S distance. The geometry of MSX3 is similar to LM2 except for an increased C–S distance.

## 2. Potential Energy Surfaces and Reaction Mechanism.

Both LM1 and LM2 are formed without a barrier from  $\text{O}(^1\text{D}) + \text{OCS}(X^1\Sigma^+)$ . The crossing from the singlet to the triplet surface might be unimportant because of the large exothermicity of these two channels. There are four branching channels from LM1: (1) decomposition to  $\text{CO}(X^1\Sigma^+) + \text{SO}(a^1\Delta)$  without well-defined TS; (2) crossing at MSX4 to the triplet surface to form  $\text{CO}(X^1\Sigma^+) + \text{SO}(X^3\Sigma^-)$ ; (3) isomerization to LM2 via TS3 with a barrier of 66.1  $\text{kJ mol}^{-1}$ , followed by decomposition to  $\text{S}(^1\text{D}) + \text{CO}_2(X^1A_1)$ ; (4) isomerizes to LM2, followed by crossing at MSX3 to the singlet surface to produce  $\text{S}(^3\text{P}) + \text{CO}_2(X^1A_1)$ . Similarly, LM2 has four branching channels to form four possible product pairs.

The reaction  $\text{O}(^3\text{P}) + \text{OCS}(X^1\Sigma^+)$  might proceed, in addition to the direct channels via TS1 and TS2 to produce  $\text{CO}(X^1\Sigma^+) + \text{SO}(X^3\Sigma^-)$  and  $\text{S}(^3\text{P}) + \text{CO}_2(X^1A_1)$ , respectively, via crossing points MSX1 and MSX2 to form LM1 and LM2, respectively, on the singlet surface, as was shown previously for the reaction  $\text{S} + \text{OCS}$ .<sup>53</sup> The subsequent paths for LM1 and LM2 are described above.

For the channel to form  $\text{CO}_2$ , the calculation indicates that the barrier at TS2 is 36.4  $\text{kJ mol}^{-1}$ , but the crossing from the triplet to the singlet curve is predicted to occur with  $\sim 3 \text{ kJ mol}^{-1}$  less energy at MSX2 that has a structure like that of TS2. For the channel to form CO, the calculation indicates that the barrier at TS1 is 27.6  $\text{kJ mol}^{-1}$ , but the crossing from the triplet to the singlet curve is predicted to occur with  $\sim 13 \text{ kJ mol}^{-1}$  less energy at MSX1 that has a structure like that of TS1. On the basis of the energy, geometry, and vibrational frequencies of OSCO at MSX1, a TST calculation gives  $k[\text{O}(^3\text{P}) + \text{OCS}] = 2.6 \times 10^{-14} \text{ cm}^3 \text{ molecule}^{-1} \text{ s}^{-1}$  at 298 K, which is near the experimental value  $1.2 \times 10^{-14} \text{ cm}^3 \text{ molecule}^{-1} \text{ s}^{-1}$ .<sup>2</sup> In fact, a slightly increased energy of MSX1 from 14.2 to 17.1  $\text{kJ mol}^{-1}$  provides quantitative account for the experimental value. This result indicates that the crossing probability for this heavy system, similar to the reaction  $\text{S} + \text{OCS}$ ,<sup>53</sup> is near unity within the  $\pm 4 \text{ kJ mol}^{-1}$  uncertainty in the predicted energy.

**E. Comparison of Observed and Predicted Results. 1. Reaction of  $\text{O}(^3\text{P}) + \text{OCS}$ .** According to calculations, the reaction of  $\text{O}(^3\text{P}) + \text{OCS}$  near room temperature is expected to proceed mainly via crossing at MSX1 to form  $\text{SO}(a^1\Delta)$  and CO. For the minor channel, the reaction is expected to proceed via crossing at MSX2 to form  $\text{S}(^1\text{D}) + \text{CO}_2$ . At higher temperature,

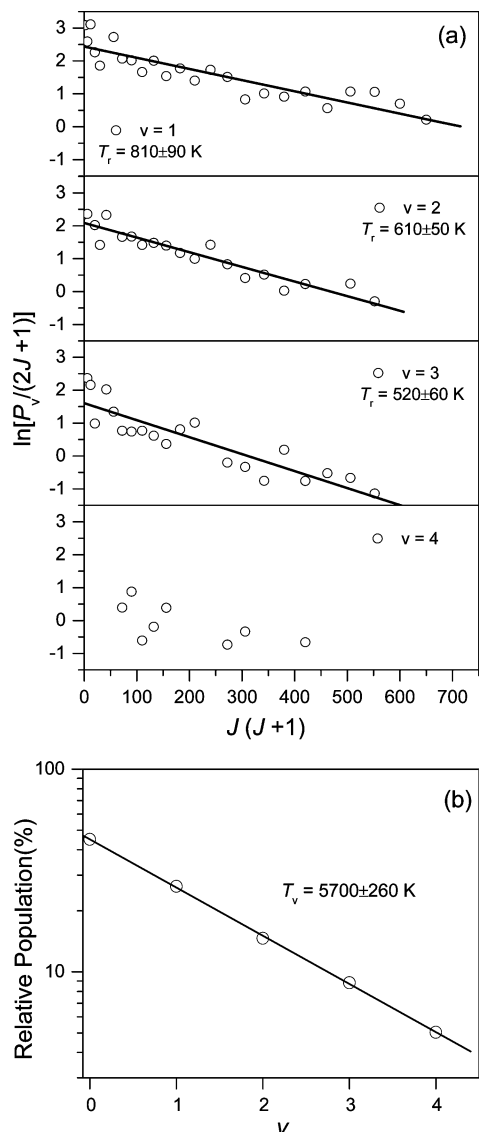


**Figure 9.** (a) Semilogarithmic plot of relative population  $P_v(J')/(2J'+1)$  as a function of  $J(J+1)$  for  $v = 1$  to 4 of CO. The slope of each line yields the rotational temperature for the respective vibrational state. (b) Semilogarithmic plot of vibrational population of CO as a function of the vibrational quantum number,  $v$ . The value for  $v = 0$  is an estimated value from linear extrapolation of the plot.

the formation of  $\text{CO} + \text{SO}$  via TS1 with energy  $\sim 13$  kJ mol $^{-1}$  greater than MSX1 must be taken into account. At even higher temperature ( $T > 1500$  K), reactions via TS1 and TS2 dominate because the crossing probabilities of MSX1 and MSX2 decrease as the velocity increases. Thermal rate coefficients predicted by Isshiki et al.<sup>6</sup> using TST with Wigner tunneling corrections are much smaller than experimental values because they did not take the crossing into account. However, predicted branching ratios are similar to experimental values at high temperatures because the crossing becomes less important.

To produce ground-state products  $\text{SO} + \text{CO}$ , LM1 must cross to the triplet surface at MSX4 before dissociation. The nearly linear O–C–S geometry of MSX4 implies that the fission of the C–S bond leads to little rotational excitation of CO but much rotational excitation of SO. The C–O bond length of MSX4 is similar to that of diatomic CO, indicating little vibrational excitation for CO product upon dissociation. In contrast, the S–O bond length of MSX4 is larger than that of SO; greater vibrational excitation of SO is hence expected. The

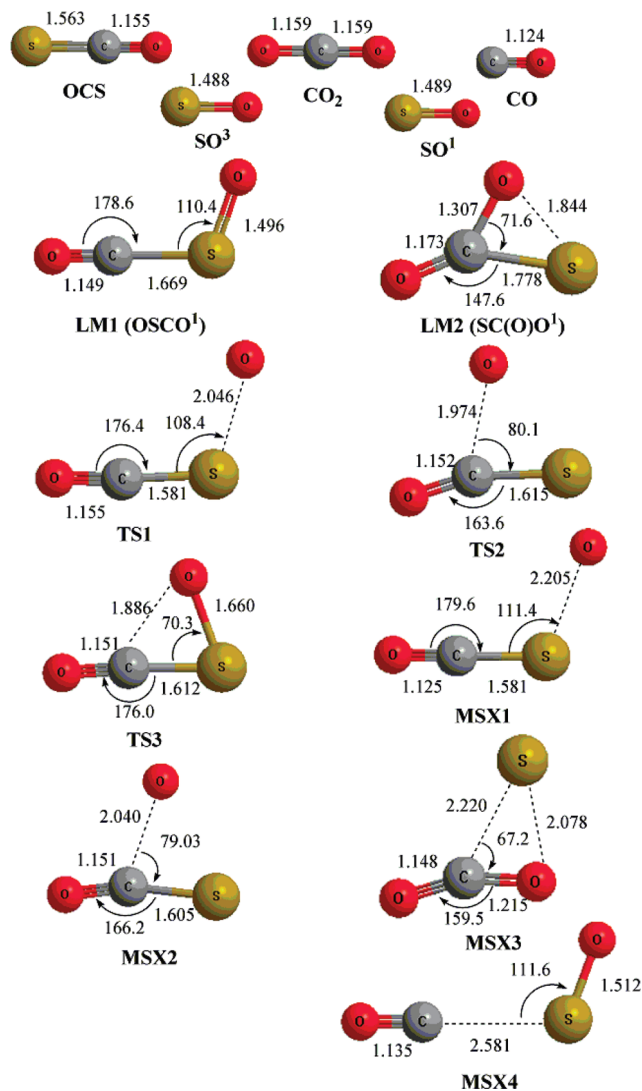


**Figure 10.** Optimized geometries of reactants, intermediates (LM), and transition states (TS) of the  $\text{O} + \text{OCS}$  system calculated at the B3LYP/6-311+G (3df) level; bond lengths are given in angstroms and bond angles are given in degrees.

vibrational distribution of SO observed by Chen et al.<sup>10</sup> and that of CO by Nickolaissen et al.<sup>9</sup> are consistent with this expectation; 26.0 and 0.6% of available energy was converted to the vibrational energies of SO and CO, respectively. The observed rotational distributions, 8.1 and 15.7% for SO and CO contradict, however, the expectation from computation; the reason is unclear. Further work on the internal distribution of CO is needed. In our experiment, we were unable to detect CO from this reaction. To produce ground-state products  $\text{S} + \text{CO}_2$ , the reaction must proceed via TS2 (36.4 kJ mol $^{-1}$ ) or via MSX2 (33.4 kJ mol $^{-1}$ ) to form LM2, followed by crossing at MSX3; the path via MSX2 likely dominates at room temperature. Both MSX3 and TS2 have a C–O distance (1.215 and 1.974 Å, respectively) much greater than that (1.159 Å) of  $\text{CO}_2$ ; high vibrational excitation of  $\text{CO}_2$  product is hence expected, which is consistent with our experimental observation. The reaction intermediate LM2 is expected to have a sufficient lifetime for intramolecular vibrational relaxation before it decomposes to  $\text{S} + \text{CO}_2$ . The observed vibrational distribution of the product  $\text{CO}_2$  is thus similar to the prior distribution assuming a statistical partitioning of the available energy. The observed  $E^*$  of  $18\,000 \pm 500$  cm $^{-1}$  ( $215 \pm 12$  kJ mol $^{-1}$ ) indicates a small contribution

**TABLE 1: Vibrational Wavenumbers and Rotational Constants for the Reactants, Intermediates (LM), Transition States (TS), Crossing Points (MSX), and Products of the  $O(^1D, ^3P) + OCS$  Reaction Computed with the B3LYP/6-311+G(3df) Method**

species	rotational constant/GHz	vibrational wavenumber/cm <sup>-1</sup>
OCS( $X^1\Sigma^+$ )	6.1	531.1, 531.1, 879.8, 2116.0
CO( $X^1\Sigma^+$ )	58.3	2216.8
SO( $a^1\Delta$ )	21.4	1156.7
SO( $X^3\Sigma^-$ )	21.4	1157.3
CO <sub>2</sub> ( $X^1A_1$ )	11.8	678.9, 678.9, 1373.9, 2413.8
LM1	29.9, 3.9, 3.4	146.0, 353.3, 533.8, 662.5, 1046.9, 2053.8
LM2	18.5, 5.5, 4.2	408.4, 555.8, 583.5, 714.2, 1067.7, 1991.91
TS1	17.0, 3.0, 3.0	244.1 <i>i</i> , 109.2, 443.8, 504.0, 829.4, 2088.6
TS2	9.5, 6.0, 3.7	363.0 <i>i</i> , 261.1, 440.4, 524.0, 797.8, 2081.9
TS3	17.2, 5.5, 4.2	470.0 <i>i</i> , 396.6, 488.5, 785.9, 831.2, 2119.2
MSX1	15.3, 3.2, 2.6	286.1 <i>i</i> , 96.7, 430.8, 455.4, 842.6, 2283.1
MSX2	10.1, 6.0, 3.7	459.6 <i>i</i> , 47.2, 448.2, 525.5, 800.5, 2098.7
MSX3	47.8, 2.8, 2.6	109.0 <i>i</i> , 299.8, 581.8, 621.5, 1403.6, 2505.7
MSX4	27.4, 2.2, 2.1	88.4 <i>i</i> , 97.4, 114.7, 167.6, 1070.5, 2125.9

from the  $S(^1D) + CO_2$  channel; that is, direct dissociation of LM2 on the singlet surface might be less important.

The quenching experiments on the reactivity of  $O(^3P)$  atoms toward OCS indicate a barrier for the channel to form  $CO_2$ , which is consistent with computed energies of TS2 (36.4 kJ mol<sup>-1</sup>) or MSX2 (33.4 kJ mol<sup>-1</sup>) to form LM2. Our estimated value of 24–29 kJ mol<sup>-1</sup> for this barrier height is smaller than, but consistent with, calculated values.

**2. Reaction of  $O(^1D) + OCS$ .** According to calculations, the reaction of  $O(^1D) + OCS$  near room temperature is expected to proceed without a barrier to form LM1 and LM2. Because of the large exothermicity, curve crossing at MSX1 or MSX2 might be unimportant. LM1 and LM2 lead to the formation of  $SO + CO$  and  $S + CO_2$ , respectively.

The intermediate LM1 has a structure OCSO in which  $\angle OCS$  is 179° and  $\angle OCS$  of the crossing point MSX4 is essentially 180°. Because of the torque exerted on CO upon fission of the C–S bond, the extent of the rotational excitation is expected to be small, which is consistent with our experiments. Similarly, the C–O bond lengths are 1.149 and 1.135 Å for LM1 and MSX4, respectively, similar to the bond length 1.124 Å of CO;

vibrational excitation of CO product is hence expected to be modest, which is consistent with our observation.

The structure of intermediate LM2 has two C–O bonds with lengths 1.173 and 1.307 Å, respectively; the latter is much greater than that (1.159 Å) calculated for  $CO_2$ . Similarly, the structure of MSX3 has two C–O bonds with lengths 1.148 and 1.215 Å, respectively. We hence expect that  $CO_2$  products via these channels are highly vibrationally excited. The observed  $E^*$  of  $30\,000 \pm 500$  cm<sup>-1</sup> ( $359 \pm 6$  kJ mol<sup>-1</sup>) is 16% greater than the available energy of 25 890 cm<sup>-1</sup> for the  $S(^1D) + CO_2$  channel but is 86% that of the 34 934 cm<sup>-1</sup> for the  $S(^3P) + CO_2$  channel. Because it is unreasonable to have  $E^*$  exceeding the available energy, we conclude that crossing at MSX3 to form  $S(^3P) + CO_2$  plays an important role. The probability of the crossing is unknown, but it might be similar to that of MSX1, close to unity, so that the triplet  $S(^3P) + CO_2$  channel dominates. The value of 86% for the triplet channel is similar to the fractions of the available energy found in the cases of  $O(^1D) + CO_2$  and  $O(^3P) + OCS$  in which the reactions proceed through a relatively long-lived complex so that the internal energy is nearly completely randomized.

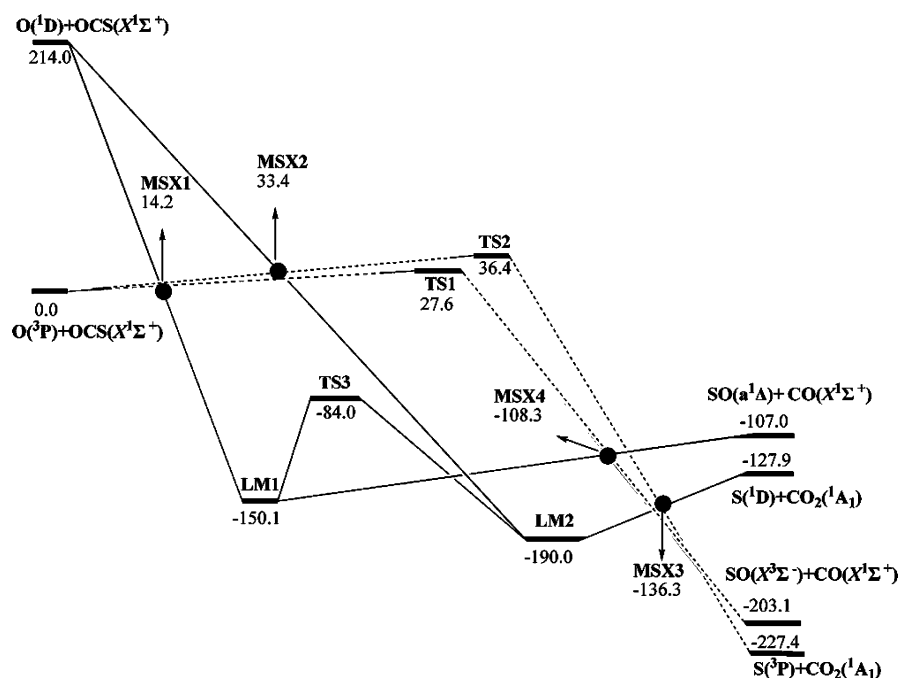


**Figure 11.** Potential energy (in kilojoules per mole) diagram for the  $O + OCS$  system calculated at the CCSD(T)//B3LYP/6-311+G (3df) level. The singlet–triplet crossing points are marked as MSX1–MSX4.



## Conclusions

We observed emission of CO and  $CO_2$  produced from reactions of  $O(^1D, ^3P) + OCS$  with time-resolved FTIR and determined their internal-state distributions. In the reaction of  $O(^3P)$  with OCS, the vibrational distribution of  $CO_2$  that yields the best fit with the observed band shape is obtained with the statistical partitioning of energy  $E^* = 18\,000 \pm 500\text{ cm}^{-1}$ , which is 85% of the available energy. The observed average vibrational energy of product  $CO_2$  corresponds to  $\sim 49\%$  of the available energy, but the observed rotational energy is  $<2\%$  of the available energy, similar to the reaction  $O(^1D) + CO_2$ . The addition of Ar quenches the reaction, indicating that the reaction proceeds with a barrier.

In the reaction of  $O(^1D)$  with OCS, the electronic-to-vibrational energy transfer for  $O(^1D) + OCS \rightarrow O(^3P) + OCS^+$  is negligible. Emission of  $OCS(0, 0^0, 1)$  was observed, which results from V–V energy transfer from highly vibrationally excited  $CO_2$ , as in the case of  $O(^3P) + OCS$ . Emissions of both CO and  $CO_2$  were observed. The vibrational distribution of  $CO_2$  is consistent with predictions using statistical partitioning of energy  $E^* = 30\,000 \pm 500\text{ cm}^{-1}$ , 86% of the available energy. The observed average vibrational energy of product  $CO_2$  corresponds to  $\sim 51\%$  of the available energy, but the observed rotational energy is  $<2\%$  of the available energy, similar to the reaction  $O(^1D) + CO_2$ .

The mechanisms of these reactions are also investigated with the CCSD(T)/6-311+G(3df)//B3LYP/6-311+G(3df) method. The results indicate that the triplet  $O(^3P) + OCS(X^1\Sigma^+)$  surface proceeds via direct abstraction and substitution channels, with barriers of 27.6 and 36.4 kJ mol $^{-1}$ , respectively, to produce  $SO(X^3\Sigma^-) + CO(X^1\Sigma^+)$  and  $S(^3P) + CO_2(X^1A_1)$ , whereas two intermediates, OSCO and SC(O)O, are formed from the singlet  $O(^1D) + OCS(X^1\Sigma^+)$  surface without a barrier, followed by decomposition to  $SO(a^1\Delta) + CO(X^1\Sigma^+)$  and  $S(^1D) + CO_2(X^1A_1)$ , respectively. For the ground state reaction  $O(^3P) + OCS(X^1\Sigma^+)$ , the singlet–triplet surface curve crossings play important roles. The major reaction channel to form  $SO + CO$  proceeds via crossing point MSX1 to form intermediate OSCO, whereas the minor channel to form  $S + CO_2$  proceeds via MSX2 to form intermediate SC(O)O. For the reaction of  $O(^1D) + OCS$  a direct formation of intermediates OSCO and SC(O)O before decomposition dominates. The observed distributions of internal states of CO and  $CO_2$  are consistent with those expected from the computed PES.

**Acknowledgment.** National Science Council of Taiwan (contract numbers NSC97-2113-M009-009-MY3) and the ATU program of the Ministry of Education, Taiwan supports this work. Calculations were performed at the National Center for High-Performance Computing, Taiwan. M.C.L. is grateful to National Science Council, Taiwan for a Distinguished Visiting Professorship and to Taiwan Semiconductor Manufacturing Co. (TSMC) for a Distinguished Professorship. S.T. is grateful to the National Science Council of Taiwan for a Distinguished Visiting Professorship at National Chiao Tung University, Hsinchu, Taiwan.

## References and Notes

- (1) Wayne, R. P. *Chemistry of Atmospheres*; Oxford University Press: Oxford, U.K., 1991.
- (2) Atkinson, R.; Baulch, D. L.; Cox, R. A.; Crowley, J. N.; Hampson, R. F.; Hynes, R. G.; Jenkin, M. E.; Kerr, J. A.; Rossi, M. J.; Troe, J. *Summary of Evaluated Kinetic and Photochemical Data for Atmospheric Chemistry*, web version, 2006.

- (3) Singleton, D. L.; Cvetanović, R. J. *J. Phys. Chem. Ref. Data* **1988**, *17*, 1377, and references therein.
- (4) Homann, K. H.; Krome, G.; Wagner, H. G. *Ber. Bunsen-Ges.* **1968**, *72*, 998.
- (5) Hsu, D. S. Y.; Shaub, W. M.; Burks, T. L.; Lin, M. C. *Chem. Phys.* **1979**, *44*, 143.
- (6) Isshiki, N.; Murakami, Y.; Tsuchiya, K.; Tezaki, A.; Matsui, H. *J. Phys. Chem. A* **2003**, *107*, 2464.
- (7) Rochford, J. J.; Powell, L. J.; Grice, R. J. *Phys. Chem.* **1995**, *99*, 15369.
- (8) Shortridge, R. G.; Lin, M. C. *Chem. Phys. Lett.* **1975**, *35*, 146.
- (9) Nickolaissen, S. L.; Veney, D. W.; Cartland, H. E. *J. Chem. Phys.* **1994**, *100*, 4925.
- (10) Chen, X.; Wu, F.; Weiner, B. R. *Chem. Phys. Lett.* **1995**, *247*, 313.
- (11) Berry, M. J. *Chem. Phys. Lett.* **1974**, *29*, 323.
- (12) Gauthier, M. J. E.; Snelling, D. R. *J. Photochem.* **1975**, *4*, 27.
- (13) Wiese, W. L.; Fuhr, J. R.; Deters, T. M. *J. Phys. Chem. Ref. Data, Monogr.* **1996**, No. 7.
- (14) Chen, H.-F.; Chiang, H.-C.; Matsui, H.; Tsuchiya, S.; Lee, Y.-P. *J. Phys. Chem. A* **2009**, *113*, 3431.
- (15) Jones, P. R.; Taube, H. *J. Phys. Chem.* **1973**, *77*, 1007.
- (16) Jaeger, K.; Weller, R.; Schrems, O. *Ber. Bunsen-Ges.* **1992**, *96*, 485.
- (17) Froese, R. D. J.; Goddard, J. D. *Mol. Phys.* **1993**, *79*, 685.
- (18) Yeh, P.-S.; Leu, G.-H.; Lee, Y.-P.; Chen, I.-C. *J. Chem. Phys.* **1995**, *103*, 4879.
- (19) Lin, S.-R.; Lee, Y.-P. *J. Chem. Phys.* **1999**, *111*, 9233.
- (20) Wu, C.-Y.; Chung, C.-Y.; Lee, Y.-C.; Lee, Y.-P. *J. Chem. Phys.* **2002**, *117*, 9785.
- (21) Yang, S.-K.; Liu, S.-Y.; Chen, H.-F.; Lee, Y.-P. *J. Chem. Phys.* **2005**, *123*, 224304.
- (22) Prahad, V.; Kumar, V. *J. Quant. Spectrosc. Radiat. Transfer* **1997**, *57*, 719.
- (23) Molina, L. T.; Lamb, J. J.; Molina, M. J. *Geophys. Res. Lett.* **1981**, *8*, 1008.
- (24) Matsumi, Y.; Kawasaki, M. *Chem. Rev.* **2003**, *103*, 4767.
- (25) DeMore, W. B.; Raper, O. *J. Phys. Chem.* **1964**, *68*, 412.
- (26) Gonzalez, C.; Schlegel, H. B. *J. Chem. Phys.* **1989**, *90*, 2154.
- (27) Frisch, M. J.; Trucks, G. W.; Schlegel, H. B.; Scuseria, G. E.; Robb, M. A.; Cheeseman, J. R.; Montgomery, J. A., Jr.; Vreven, T.; Kudin, K. N.; Burant, J. C.; Millam, J. M.; Iyengar, S. S.; Tomasi, J.; Barone, V.; Mennucci, B.; Cossi, M.; Scalmani, G.; Rega, N.; Petersson, G. A.; Nakatsuji, H.; Hada, M.; Ehara, M.; Toyota, K.; Fukuda, R.; Hasegawa, J.; Ishida, M.; Nakajima, T.; Honda, Y.; Kitao, O.; Nakai, H.; Klene, M.; Li, X.; Knox, J. E.; Hratchian, H. P.; Cross, J. B.; Bakken, V.; Adamo, C.; Jaramillo, J.; Gomperts, R.; Stratmann, R. E.; Yazyev, O.; Austin, A. J.; Cammi, R.; Pomelli, C.; Ochterski, J. W.; Ayala, P. Y.; Morokuma, K.; Voth, G. A.; Salvador, P.; Dannenberg, J. J.; Zakrzewski, V. G.; Dapprich, S.; Daniels, A. D.; Strain, M. C.; Farkas, O.; Malick, D. K.; Rabuck, A. D.; Raghavachari, K.; Foresman, J. B.; Ortiz, J. V.; Cui, Q.; Baboul, A. G.; Clifford, S.; Cioslowski, J.; Stefanov, B. B.; Liu, G.; Liashenko, A.; Piskorz, P.; Komaromi, I.; Martin, R. L.; Fox, D. J.; Keith, T.; Al-Laham, M. A.; Peng, C. Y.; Nanayakkara, A.; Challacombe, M.; Gill, P. M. W.; Johnson, B.; Chen, W.; Wong, M. W.; Gonzalez, C.; Pople, J. A. *Gaussian 03*, revision C.01; Gaussian, Inc.: Wallingford, CT, 2004.
- (28) Yamamoto, N.; Vreven, T.; Robb, M. A.; Frisch, M. J.; Schlegel, H. B. *Chem. Phys. Lett.* **1996**, *250*, 373.
- (29) Chedin, A. *J. Mol. Spectrosc.* **1979**, *761*, 430.
- (30) Tashkun, S. A.; Perevalov, V. I.; Teffo, J.-L.; Rothman, L. S.; Tynnterev, V. I. *J. Quant. Spectrosc. Radiat. Transfer* **1998**, *60*, 785.
- (31) Levine, R. D.; Bernstein, R. B. *Molecular Reaction Dynamics and Chemical Reactivity*; Oxford University Press: New York, 1985.
- (32) Western, C. M. *PGOPHER*, a program for simulating for rotational structure. <http://pgopher.chm.bris.ac.uk>.
- (33) Kanamori, H.; Butler, J. E.; Kawaguchi, K.; Yamada, C.; Hirota, E. *J. Chem. Phys.* **1985**, *83*, 611.
- (34) Kolbe, W. F.; Leskovar, B. *J. Chem. Phys.* **1986**, *85*, 7117.
- (35) Chen, X.; Asmar, F.; Wang, H.; Weiner, B. R. *J. Phys. Chem.* **1991**, *95*, 6415.
- (36) Yamasaki, K.; Taketani, F.; Sugiura, K.; Tokue, I.; Tsuchiya, K. *J. Phys. Chem. A* **2004**, *108*, 2382.
- (37) Felder, P.; Effenhauser, C. S.; Haas, B. M.; Huber, J. R. *Chem. Phys. Lett.* **1988**, *148*, 417.
- (38) Felder, P.; Haas, B.-M.; Huber, J. R. *Chem. Phys. Lett.* **1993**, *204*, 248.
- (39) Kawasaki, M.; Sato, H. *Chem. Phys. Lett.* **1987**, *139*, 585.
- (40) Brouard, M.; Cireasa, R.; Clark, A. P.; Preston, T. J.; Vallance, C.; Groenenboom, G. C.; Vasyutinskii, O. S. *J. Phys. Chem. A* **2004**, *108*, 7965.
- (41) Stephenson, J. C.; Wood, R. E.; Moore, C. B. *J. Chem. Phys.* **1968**, *48*, 4790.
- (42) Finzi, J.; Moore, C. B. *J. Chem. Phys.* **1975**, *63*, 2285.

- (43) Abe, M.; Sato, Y.; Inagaki, Y.; Matsumi, Y.; Kawasaki, M. *J. Chem. Phys.* **1994**, *101*, 5647.
- (44) Chase, M. W., Jr. *J. Phys. Chem. Ref. Data, Monogr.* **1998**, No. 9.
- (45) Matsumi, Y.; Inagaki, Y.; Morley, G. P.; Kawasaki, M. *J. Chem. Phys.* **1994**, *100*, 315.
- (46) Thelen, M.-A.; Gejo, T.; Harrison, J. A.; Huber, J. R. *J. Chem. Phys.* **1995**, *103*, 7946.
- (47) Matsumi, Y.; Shamsuddin, S. M.; Sato, Y.; Kawasaki, M. *J. Chem. Phys.* **1994**, *101*, 9610.
- (48) Perri, M. J.; Van Wyngarden, A. L.; Boering, K. A.; Lin, J. J.; Lee, Y. T. *J. Chem. Phys.* **2003**, *119*, 8213.
- (49) Perri, M. J.; Van Wyngarden, A. L.; Lin, J. J.; Lee, Y. T.; Boering, K. A. *J. Phys. Chem. A* **2004**, *108*, 7995.
- (50) Wu, C.-Y.; Lee, Y.-P.; Ogilvie, J. F.; Wang, N. S. *J. Phys. Chem. A* **2003**, *107*, 2389.
- (51) Chen, H.-F.; Lee, Y.-P. *J. Phys. Chem. A* **2006**, *110*, 12096.
- (52) Setzer, K. D.; Fink, E. H.; Ramsay, D. A. *J. Mol. Spectrosc.* **1999**, *198*, 163.
- (53) Lu, C.-W.; Wu, Y.-J.; Lee, Y.-P.; Zhu, R. S.; Lin, M. C. *J. Chem. Phys.* **2006**, *125*, 164329.

JP903976Z